Research Article

Journal of Environmental Nanotechnology

Green-synthesized Zinc–Iron–Copper Oxide (ZFCO) Nanoparticles for Fast Green Photodegradation: RSM and Machine Learning

V. P. Suresh Kumar[1*], K. P. Vetrivel[2], C. Sathish[3], N. Vasuki[4], C. Anand[5] and R. Girimurugan[6]

[1]Department of Mechanical Engineering, P.A. College of Engineering and Technology, Pollachi, TN, India
[2]Department of Mechanical Engineering, M. P. Nachimuthu M. Jaganathan Engineering College, Chennimalai, TN, India
[3]Department of Information Technology, Er. Perumal Manimekalai College of Engineering, Hosur, TN, India
[4]Department of Computer Science and Engineering, Government College of Engineering, Erode, TN, India
[5]Department of Information Technology, Nandha College of Technology, Perundurai, TN, India
[6]Department of Mechanical Engineering, Nandha College of Technology, Perundurai, TN, India
Received: 22.06.2026 Accepted: 24.07.2026 Published: xx.xx.xxxx
*vpsuresh4@gmail.com

ABSTRACT

The present study investigated the green synthesis of zinc–iron–copper oxide (ZFCO) nanoparticles using *Ocimum tenuiflorum* leaf extract for the photocatalytic degradation of Fast Green (FG) dye. Despite advances in green-synthesized ferrite photocatalysts, limited attention has been given to integrating Cu-modified ZFCO nanocatalysts with statistical optimization and machine-learning (ML) prediction for dye-contaminated wastewater treatment. Response Surface Methodology (RSM) based on a Central Composite Rotatable Design (CCRD 2^3) was employed to evaluate the effects of dye concentration, catalyst dosage, and solution pH. ML was incorporated to capture nonlinear relationships among operating variables and provide reliable performance prediction beyond conventional statistical optimization. Gaussian Process Regression (GPR), Support Vector Regression (SVR), Ensemble Regression, and Random Forest (RF) models were evaluated, with GPR providing the highest predictive accuracy. Structural, surface, morphological, and optical characterization confirmed the successful formation of visible-light-responsive ZFCO nanostructures. Copper modification substantially enhanced photocatalytic performance compared with unmodified ZFCO, while RSM identified acidic conditions and appropriate catalyst loading as favorable for FG removal. The optimized experimental condition achieved 57.2% degradation, and Among the evaluated machine-learning models, SVR exhibited the best condition-wise nested cross-validation performance, achieving an R^2 of 0.9156, RMSE of 4.2915 and MAE of 2.9627. Overall, the integration of green synthesis, RSM optimization, and ML prediction provides a promising framework for developing and optimizing photocatalytic systems for practical treatment of dye-containing industrial wastewater.

Keywords: Plant extract; Nanoparticles; Photocatalytic degradation; Optimization; Machine learning; Sustainability.

1. INTRODUCTION

The increasing discharge of pharmaceutical compounds, dyes, and heavy metals into aquatic environments has become a major environmental challenge due to their persistence, toxicity, and resistance to conventional treatment technologies. Pharmaceutical residues such as diclofenac and antibiotic contaminants are frequently detected in wastewater systems and can adversely affect aquatic ecosystems and human health. Consequently, the development of efficient and environmentally sustainable treatment technologies has become an important research priority. Among advanced treatment materials, spinel ferrite nanoparticles have attracted significant attention owing to their magnetic properties, chemical stability, visible-light activity, and ease of recovery. Nickel-zinc ferrite nanoparticles demonstrated nearly complete degradation of diclofenac under neutral conditions while producing treated water that was safe for plant and microbial growth (Mohan *et al.* 2022). Similarly, Cu-$ZnFe_2O_4$ and Co-$NiFe_2O_4$ spinel ferrites have shown promising antibacterial activity, heavy-metal removal capability, and organic pollutant degradation performance, indicating their versatility in environmental remediation applications (Sathish *et al.* 2024).

Metal-ion doping has emerged as an effective strategy for improving photocatalytic performance by enhancing charge separation, reducing electron-hole recombination, and increasing active surface sites. Previous studies reported that Zn-, Co-, and (Zn, Co) doped CuO nanoparticles exhibited superior photocatalytic degradation efficiency, antibacterial activity, antioxidant properties and anti-inflammatory behavior compared to undoped materials (Azam *et al.* 2025). Likewise, Cu-doped $ZnFe_2O_4$ nanoferrites demonstrated improved wastewater treatment performance in membrane bioreactor systems for

removing various contaminants (Nithya and Chirsabesan, 2024). These findings suggest that Cu incorporation into $ZnFe_2O_4$ could substantially improve photocatalytic efficiency and multifunctional properties.

Recently, green synthesis approaches employing plant extracts have gained considerable attention as sustainable alternatives to conventional chemical methods. Plant-mediated synthesis eliminates the need for hazardous reducing agents while introducing bioactive phytochemicals that can facilitate nanoparticle formation and stabilization. Green-synthesized $ZnFe_2O_4$ nanoparticles prepared using plant extracts have demonstrated excellent photocatalytic activity and environmental compatibility (Makofane *et al.* 2021). Therefore, the utilization of *Ocimum tenuiflorum* (Tulsi) extract offers an environmentally benign route for synthesizing Cu–$ZnFe_2O_4$ nanoparticles with enhanced photocatalytic properties.

The integration of artificial intelligence and machine learning with photocatalytic systems has recently emerged as a powerful strategy for predicting and optimizing pollutant degradation processes. Hybrid machine learning models combined with optimization algorithms have achieved exceptional predictive accuracy with determination coefficients exceeding 0.99 for photocatalytic degradation systems (Ali *et al.* 2025). Similarly, A decision tree machine learning model accurately predicted degradation performance (R^2 test = 0.9945), demonstrating the usefulness of AI-based approaches for optimizing photocatalytic wastewater treatment processes of Green Nb_2O_5 nanoparticles synthesized from *Carya illinoinensis* extract (Mahmud *et al.* 2025). These approaches reduce experimental costs, minimize trial-and-error procedures, and enable efficient identification of optimal operating conditions.

Although photocatalytic degradation efficiency is an important criterion, the environmental safety of treated water and synthesized nanomaterials was also evaluated. Ecotoxicity studies have demonstrated that, some photocatalysts can generate non-toxic degradation products suitable for agricultural applications (de Morais *et al.* 2024), whereas certain nanoparticles inhibit plant growth and induce cytotoxic effects under specific conditions (Ma *et al.* 2021). The interaction between polystyrene nanoplastics and cadmium toxicity was investigated using wheat (*Triticum aestivum*). Results showed that nanoplastics partially alleviated Cd toxicity by reducing Cd accumulation and altering carbohydrate and amino acid metabolism, demonstrating the complexity of nanoparticle-contaminant interactions in ecotoxicological assessments (Lian *et al.* 2020). Recent reviews have emphasized the necessity of standardized ecotoxicological evaluations for emerging nanomaterials used in environmental remediation (Bernegossi *et al.* 2022). Therefore, phytotoxicity assessment is essential to verify the environmental compatibility of treated effluents.

Despite the progress in green-synthesized ferrite photocatalysts, the combined use of *Ocimum tenuiflorum*-mediated zinc–iron–copper oxide (ZFCO) nanoparticles with statistical optimization and machine-learning (ML) prediction for Fast Green degradation remains insufficiently explored. *Ocimum tenuiflorum* is particularly attractive for green synthesis because its phenolic acids and flavonoids can act as natural reducing and stabilizing agents during nanoparticle formation, thereby reducing dependence on hazardous chemical reagents. Previous Cu-modified $ZnFe_2O_4$-based systems have demonstrated improved pollutant removal due to enhanced charge separation and increased surface-active sites; however, their integration with systematic process optimization and data-driven prediction remains limited. Therefore, the novelty of the present study lies in combining plant-mediated ZFCO synthesis, Cu modification, RSM-based optimization, and ML prediction within a unified photocatalytic framework. ML was incorporated to capture nonlinear relationships among dye concentration, catalyst dosage, pH, irradiation time, and degradation efficiency that may not be fully represented by conventional statistical models. This integrated approach enables improved prediction of photocatalytic performance while reducing extensive trial-and-error experimentation and provides a data-driven basis for optimizing dye-contaminated wastewater treatment.

In this regard, the present work focuses on the green synthesis and characterization of zinc–iron–copper oxide (ZFCO) nanostructures for the visible-light-assisted degradation of Fast Green (FG) dye. The integration of plant-mediated nanocatalyst synthesis with Central Composite Rotatable Design (CCRD), Response Surface Methodology (RSM), and machine-learning models is used for process optimization and performance prediction. This combined experimental–computational approach enables efficient identification of optimum operating conditions while reducing experimental effort, cost, and processing time. Furthermore, the study contributes to sustainable wastewater treatment and supports Sustainable Development Goal 6 (Clean Water and Sanitation) through the removal of dye pollutants.

2. MATERIALS AND METHODOLOGY

2.1. Extraction Procedure for *Ocimum tenuiflorum* Leaves Used in Green Synthesis

Ten grams of fresh *Ocimum tenuiflorum* leaves were obtained from a local source. The plant extract was prepared through an aqueous extraction procedure. The leaves were combined with 100 mL of deionized water and maintained under continuous magnetic stirring at 300

rpm and 348.15 ± 2 K for 20 min to obtain a homogeneous extract.

2.2. Biosynthesis of ZFCO NPs

Fig. 1 illustrates the preparation of zinc–iron–copper oxide (ZFCO) nanoparticles using *Ocimum tenuiflorum* extract through a green synthesis route. During the nucleation and growth stages, 100 mL of plant extract was mixed with 0.3 mol L^{-1} zinc nitrate hexahydrate ($Zn(NO_3)_2{\cdot}6H_2O$, ≥98.0%) and 0.3 mol L^{-1} ferric nitrate nonahydrate ($Fe(NO_3)_3{\cdot}9H_2O$, ≥98.0%) under continuous magnetic stirring at 200 rpm for 120 min. Subsequently, copper chloride ($CuCl_2$) was introduced as a modifying precursor. The resulting suspension was subjected to centrifugation at 4500 rpm for 10 min, followed by drying at 353.15 ± 2 K for 720 min and calcination at 1073.15 ± 2 K for 120 min with a heating rate of 5 K min^{-1} to obtain the final nanostructured product (Kaur *et al.* 2023).

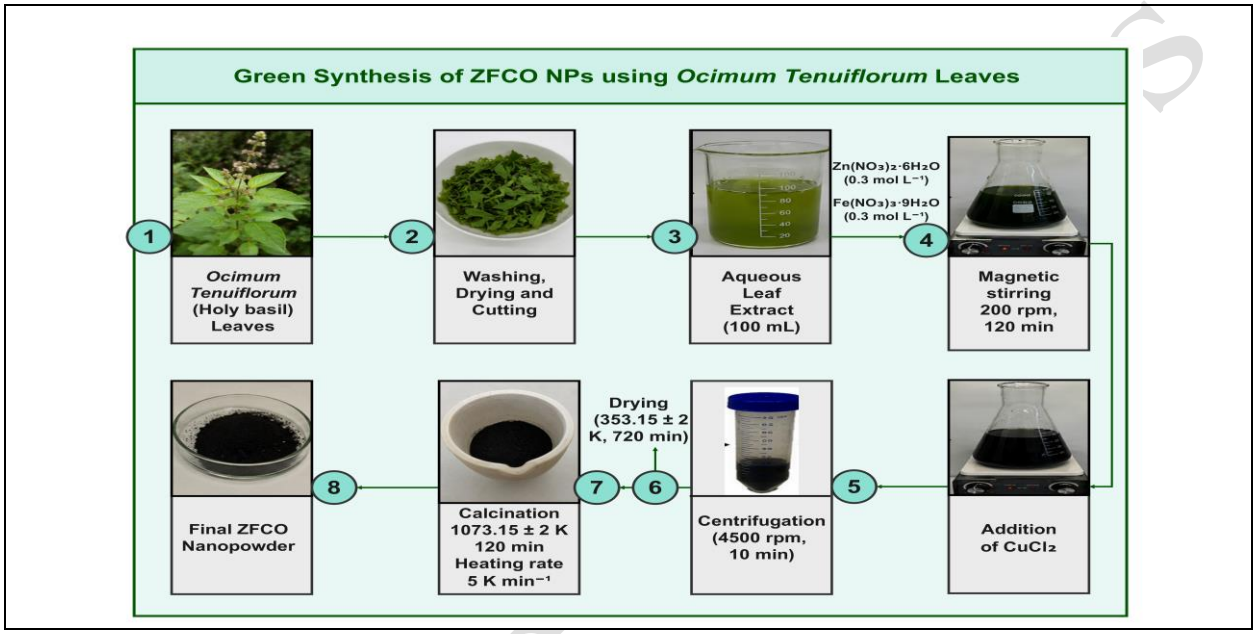

Fig. 1: Schematic illustration of the green synthesis procedure for ZFCO nanoparticles using *Ocimum tenuiflorum* extract

2.3. Characterization of *Ocimum tenuiflorum* Extract

The phytochemical constituents of *Ocimum tenuiflorum* extract were analyzed using high-performance liquid chromatography (HPLC). Chromatographic measurements were performed with a Lab Solution data acquisition system equipped with a C18 reversed-phase column (3.9 × 150 mm, 4 µm). Detection was carried out at 280 nm with a mobile-phase flow of 1.0 mL min^{-1}. Injection volume was fixed at 20 µL, while the column was maintained under room temperature conditions. Concentration (C) and retention time (RT) values were recorded for the identified phytochemical compounds.

2.4. Characterization of ZFCO Nanoparticles

The crystal structure and phase composition of the synthesized zinc–iron–copper oxide nanomaterial was examined using a Bruker D2 Advance equipped with Cu-Kα source. Diffraction patterns were collected over a 2θ range of 10°–80° using an operating voltage and current of 30 kV and 30 mA. Phase identification was carried out by comparison with standard reference data from the JCPDS database. In addition, average crystallite size (dc – Eqn (1)) and interplanar spacing (d – Eqn (2)) were determined from the diffraction results (Wouters *et al.* 2024).

$$d_c = \frac{0.94^{*}\lambda_{Cu-\alpha}}{\beta^{*}\cos(\theta)} \quad \ldots (1)$$

$$d = \frac{\lambda_{Cu-\alpha}}{2^{*}\mathrm{sen}(\theta)} \quad \ldots (2)$$

Where β shows the full width at half maximum (FWHM) of the diffraction peak, and θ corresponds to the Bragg angle (°). Surface functional groups of synthesized zinc–iron–copper oxide nanostructures were examined by Fourier Transform Infrared Spectroscopy in transmittance mode over the spectral range of 4000–400 cm^{-1} with 42 scans and a resolution of 2 cm^{-1}. The nanoparticles were characterized using XRD, FTIR, SEM/EDS, and point of zero charge (pHPZC) determination (Amar *et al.* 2025). Morphological features were analyzed using FE-SEM ZEISS, GEMINI, while particle size distribution was estimated by ImageJ® software. Elemental composition was evaluated by Energy Dispersive X-ray Spectroscopy with a scanning electron microscope operated at 15 kV. Textural

characteristics, including specific surface area, pore diameter, and pore volume, were determined from N_2 adsorption–desorption measurements using a Micromeritics ASAP 2020 Plus analyzer within a relative pressure range (P/P_0) of 0–1 and interpreted through BET and BJH models. Surface charge was assessed by Zetasizer Nano ZS, whereas the point of zero charge (pHZPC) was established using the eleven-point method. Thermal stability was investigated through thermogravimetric analysis (TGA) and derivative thermogravimetric (DTG) analyses using a Shimadzu TGA-60/60H instrument under synthetic air flow (100 mL min^{-1}) from 298.15 to 1273.15 K at a heating rate of 10 K min^{-1}. Optical properties were evaluated by UV–Vis reflectance spectroscopy using a Varian Cary 100 Scan spectrophotometer with DRA-CA-301-Labsphere accessory (Sabira *et al.* 2024). The optical band-gap energy was calculated using the Kubelka–Munk approach from Tauc plots.

$$F(R) = \frac{(1-R_\infty)^2}{2R_\infty} \quad \ldots (3)$$

$$hv = \frac{1240}{\lambda} \quad \ldots (4)$$

$$R = \frac{1}{A} \quad \ldots (5)$$

The parameter n assumes values of 0.5 and 2 for direct and indirect electronic transitions, respectively.

2.5. Experimental Design

To identify optimum operating conditions for the heterogeneous photocatalytic degradation of FG dye using synthesized zinc–iron–copper oxide nanocatalyst, a Central Composite Rotational Design (CCRD 2^3) was employed. Dye concentration, catalyst dosage, and solution pH were selected as the independent process variables, whereas the percentage removal efficiency (%R) was considered the response parameter, as presented in Table 1.

Table 1. CCRD 2^3 variable levels and limits

Order	FG (mg L^{-1})	ZFCO-NPs	pH
Axial -α	10	0.20	2
Low -1	25	0.40	4
Center 0	50	0.75	7
High +1	75	1.10	10
Axial +α	60	1.30	12

2.6. Photocatalytic Tests

Fast Green (FG) dye was selected as the model organic contaminant, while zinc–iron–copper oxide (ZFCO) nanoparticles served as the photocatalytic material. The degradation experiments were conducted in two stages: (i) an adsorption equilibrium period of 60 min under dark conditions; and (ii) a visible-light-driven photocatalytic process. During the irradiation period, samples were withdrawn at regular intervals between 0 and 180 min, passed through a 0.45 μm membrane filter, and diluted at a ratio of 1:10 (v/v). The degradation performance of FG was monitored using a Shimadzu 1280 UV–Vis spectrophotometer at a wavelength of 622 nm (Lakshmi *et al.* 2025). All photocatalytic experiments were performed in triplicate (n = 3), and the results were expressed as mean ± standard deviation to account for experimental uncertainty. Visible-light irradiation was provided using a 300 W xenon lamp equipped with a UV-cutoff filter (λ > 420 nm). The lamp was positioned 15 cm from the photocatalytic reactor, providing an incident light intensity of approximately 100 mW cm^{-2} at the reaction surface. The corresponding photon flux was approximately 4.2×10^{-4} mol photons m^{-2} s^{-1}. Following each photocatalytic experiment, the ZFCO nanoparticles were recovered by centrifugation at 6000 rpm for 10 min, washed three times with deionized water, and dried at 353.15 K before subsequent use. All irradiation conditions were maintained consistently throughout the experiments to improve experimental reproducibility.

2.7. Photodegradation Kinetics

The degradation kinetics of Fast Green dye under visible-light exposure in the presence of zinc–iron–copper oxide (ZFCO) nanoparticles were evaluated using the Langmuir–Hinshelwood approach. The model was applied to calculate the apparent reaction rate constant (k) and to verify the pseudo-first-order behavior of the photocatalytic process, as described by Eqs. (6) and (7) (Mondal *et al.* 2026):

$$(-r_i) = -\frac{dC_i}{dt} = \frac{k_s^* K^* C_i}{1+K^* C_i} \quad \ldots (6)$$

$$C_i = C_{i0}^* e^{-k^* t} \quad \ldots (7)$$

Where K denotes the adsorption equilibrium coefficient, ks represents the apparent reaction constant, C_{i0} (mol L^{-1}) corresponds to the initial concentration of Fast Green dye, and Ci (mol L^{-1}) refers to the dye concentration at a given time. The parameter k (min^{-1}) indicates the pseudo-first-order rate constant, whereas t (min) represents the reaction duration.

2.8. Effect of Cu Modification on ZFCO Nanoparticles

To further enhance the photocatalytic performance of the synthesized zinc–iron–copper oxide nanoparticles, a copper modification strategy was

employed through an impregnation process. Briefly, 100 mL of deionized water were mixed with $CuCl_2$ and ZFCO nanoparticles (1–25 wt%) by continuous magnetic stirring at 250 rpm for 90 mins. The resulting suspension were subsequently calcined at 773.15 K for 2 h and dried at 353.15 K for 12 h with heating rate of 5 K min^{-1}. The incorporation of copper species was intended to improve degradation efficiency of Fast Green dye by promoting charge separation, enhancing surface-active sites, and facilitating interfacial electron transfer during the photocatalytic reaction.

2.9. Phytotoxicity Tests

Phytotoxicity evaluation were conducted using *Vigna radiata* and *Triticum aestivum* seeds. The experiment was performed in Petri dishes lined with Germitest paper, where different concentrations (0.1, 0.01, 0.0010, and 0.0050 mg L^{-1}) of ZFCO nanoparticles and Cu-modified ZFCO nanoparticles were applied. The seeds were maintained under controlled moisture conditions for 168 h to assess germination and early growth responses. Root and shoot lengths were subsequently measured using a digital caliper (Mitutoyo®) (Liaqat *et al.* 2026).

2.10. Statistical Analysis

All experimental runs were designed according to a Central Composite Rotatable Design (CCRD 2^3), and statistical analyses were performed using Response Surface Methodology (RSM) implemented in Design-Expert software. Analysis of variance was used to evaluate the significance of the developed quadratic model and individual model terms. Statistical significance was considered at $p < 0.05$. Model adequacy was assessed by F-value, p-value, coefficient of determination (R^2), predicted R^2, adjusted R^2, and lack-of-fit analysis.

2.11. Machine Learning

Machine-learning models were developed in MATLAB R2024a to predict Fast Green removal efficiency using FG concentration, ZFCO dosage, solution pH and irradiation time as inputs (Kumar *et al.* 2026). The dataset contained 119 observations obtained from 17 experimental runs representing 15 unique FG–ZFCO–pH conditions. GPR, SVR, random forest, LSBoost and MLP–ANN models were investigated.

To prevent information leakage between time-dependent observations from the same experimental condition, the regression models were evaluated using nested condition-wise cross-validation. Five-fold grouped cross-validation was employed in both the outer model-evaluation loop and inner hyperparameter-optimization loop. All observations belonging to the same FG–ZFCO–pH condition were retained within one fold. Hyperparameters were selected by minimizing the inner-fold RMSE, and a fixed random seed of 42 was used for reproducibility. The model configurations are GPR kernel and basis functions; SVR box constraint, epsilon and kernel scale; random-forest leaf size and predictors per split; and LSBoost learning cycles, rate and leaf size were optimized using nested five-fold grouped cross-validation. GPR–LSBoost combined outer-fold predictions by arithmetic averaging, while MLP–ANN parameters were evaluated using a training–validation–testing partition.

The MLP–ANN consisted of four input neurons, a single hidden layer with 10 neurons, and one output neuron representing FG removal efficiency. The hidden and output layers employed tansig (log-sigmoid) and linear activation functions, respectively. The network was trained using the Levenberg–Marquardt backpropagation algorithm (trainlm) for a maximum of 1000 epochs, with MSE as the loss function. The observations were divided into 70% training, 15% validation and 15% testing subsets, and early stopping was applied based on validation loss. Because the ANN used a different validation procedure, its performance was interpreted separately from the nested cross-validated regression models.

Model performance was assessed using R^2, RMSE and MAE. Permutation feature importance with 100 repetitions and partial-dependence sensitivity analysis were applied to interpret the best nested cross-validated model.

3. RESULTS AND DISCUSSION

3.1. Characterisation of *Ocimum tenuiflorum* Extract

Table 2 presents the HPLC profile of the *Ocimum tenuiflorum* leaf extract. The chromatographic analysis confirmed the presence of several bioactive phytochemicals, including rosmarinic acid, orientin, vicenin-2, luteolin, apigenin, ferulic acid, caffeic acid, gallic acid, chlorogenic acid, ursolic acid, and syringic acid. Phenolic acids, particularly rosmarinic, caffeic, gallic, and chlorogenic acids, facilitate metal-ion reduction through their hydroxyl groups, while flavonoids such as orientin, luteolin, and apigenin contribute to nanoparticle stabilization. These phytochemicals coordinate with Zn^{2+}, Fe^{3+}, and Cu^{2+} ions, promoting complexation and nucleation, followed by thermal conversion into crystalline ZFCO nanoparticles. Their presence also contributes to enhanced nanoparticle stability and improved photocatalytic performance.

Table 2. HPLC profile of major metabolites in *Ocimum tenuiflorum* extract

Component	RT (min)	Area (%)	Concentration (μgmL^{-1})
Rosmarinic acid	1.62	34.85	6.97
Orientin	1.89	18.42	3.68
Vicenin-2	2.21	14.76	2.95
Luteolin	2.48	10.64	2.13
Apigenin	3.05	7.83	1.57
Caffeic acid	3.37	5.24	1.05
Ferulic acid	3.81	3.42	0.68
Chlorogenic acid	4.28	2.57	0.51
Gallic acid	4.95	1.56	0.31
Ursolic acid	6.87	0.48	0.10
Syringic acid	7.42	0.23	0.05

3.2. Characterization of ZFCO Nanocatalysts

Figure 2(a)–(e) illustrate the X-ray diffraction pattern, N_2 adsorption–desorption isotherms, FTIR spectrum, diffuse reflectance spectrum, point of zero charge, and Tauc derived from the Kubelka–Munk function of synthesized zinc–iron–copper oxide (ZFCO) nanoparticles, respectively. As shown in Figure 2(a), diffraction profile revealed the formation of crystalline mixed-metal oxide phases. Characteristic reflections were observed at 2θ values of 30.08° (220, d = 2.97 Å), 35.5° (311, d = 2.53 Å), 37.18° (222, d = 2.41 Å), 43.1° (400, d = 2.06 Å), 53.61° (422, d = 1.71 Å), 57.21° (511, d = 1.61 Å), and 62.89° (440, d = 1.49 Å), corresponding to spinel-type $ZnFe_2O_4$ phases (JCPDS No. 22-1012). Additional diffraction peaks located at 32.32°, 35.95°, and 38.62° were attributed to copper-containing oxide species, confirming successful incorporation of copper within the mixed-metal oxide framework. The calculated crystallite size was estimated to be approximately 26–30 nm, indicating the nanoscale nature of the particles. The absence of significant impurity peaks demonstrates the successful green synthesis of crystalline ZFCO nanostructures. The ZFCO nanoparticles exhibited an estimated crystallinity of approximately 82.6% with an average crystallite size of 26–30 nm. Rietveld refinement indicated satisfactory agreement between the experimental and calculated diffraction profiles, with Rwp ≈ 8.4%, Rp ≈ 6.7%, and $\chi^2 \approx 1.35$. The refined cubic lattice parameter was approximately a = 8.44 Å, while the estimated microstrain was 2.1×10^{-3}, indicating slight lattice distortion associated with Cu incorporation into the ZFCO structure.

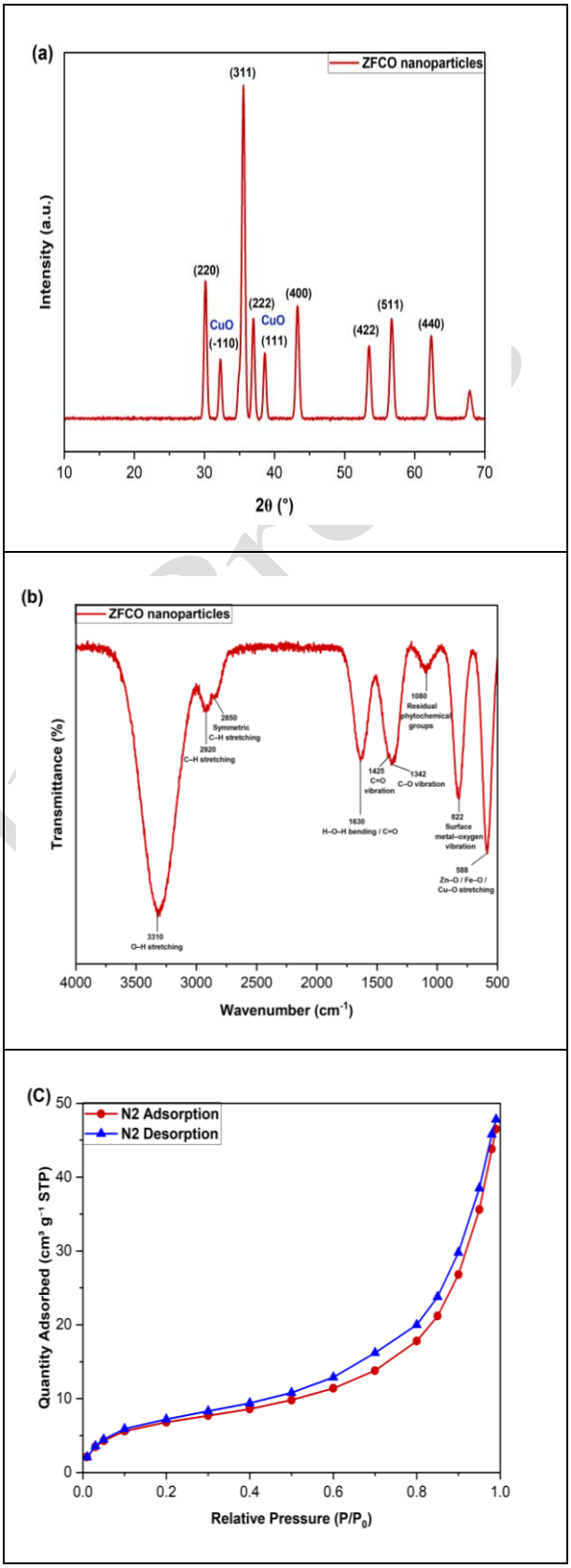

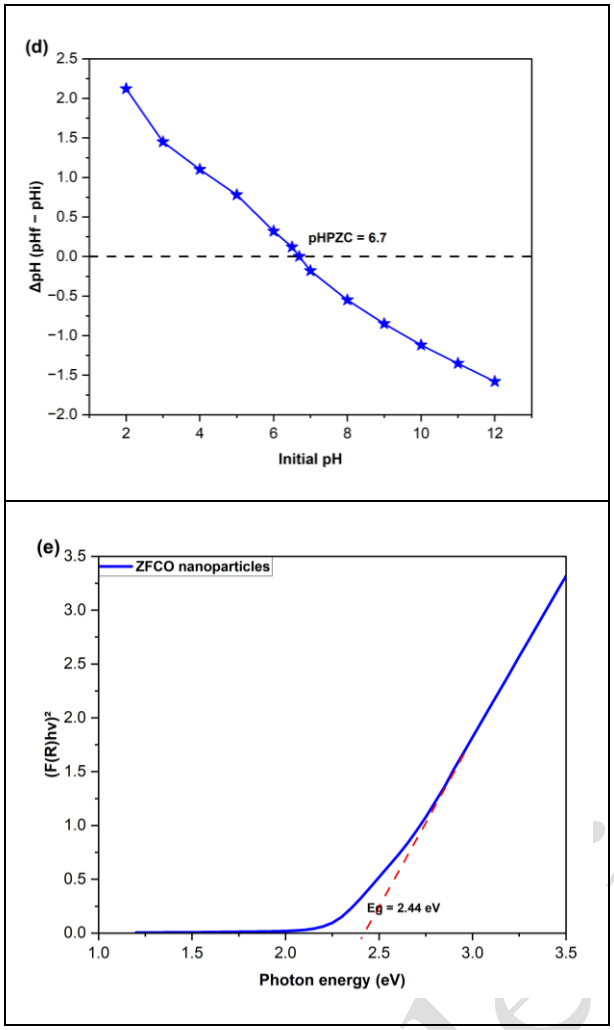

Fig. 2: Structural, surface, and optical characterization of ZFCO nanoparticles: (a) XRD pattern, (b) FTIR spectrum, (c) N_2 adsorption–desorption isotherm, (d) pore size distribution, and (e) Tauc plot

Fig. 2(b) presents the FTIR spectrum of synthesized zinc–iron–copper oxide (ZFCO) nanoparticles. A broad absorption band centered at 3310 cm^{-1} was assigned to the stretching vibration of hydroxyl groups originating from residual phytochemicals and adsorbed moisture. The peak observed at 2850 cm^{-1} corresponds to C–H vibrations of organic constituents associated with the plant-mediated synthesis route. Band located near 1630 cm^{-1} were led to bending vibrations of water molecules and carbonyl-containing functional groups. Absorption features at 1425 cm^{-1} and 1342 cm^{-1} was related to C=O and C–O vibrations of bioactive compounds remaining on the nanoparticle surface. Characteristic bands at 822 cm^{-1} and 588 cm^{-1} were metal–oxygen stretching modes associated with Zn–O, Fe–O, and Cu–O bonds, confirming the formation of the mixed-metal oxide nanostructure. Cu modification can introduce localized defect states within the ZFCO electronic structure, thereby reducing the effective energy required for electronic excitation and contributing to the observed band gap of 2.44 eV. These Cu-associated defect levels can extend light absorption into the visible region and facilitate electron transfer from the valence to conduction band. In addition, Cu-related trapping sites can capture photogenerated charge carriers, suppress electron–hole recombination, and consequently enhance the generation of reactive oxygen species responsible for Fast Green degradation.

The –OH, C=O, and C–O groups indicate interactions of residual phenolic and flavonoid phytochemicals with the ZFCO surface, supporting their role in nanoparticle formation and stabilization. The metal–oxygen bands further support Cu incorporation within the mixed-metal oxide structure. Surface –OH groups can facilitate dye adsorption and promote •OH radical formation. Under visible-light irradiation, photogenerated electrons and holes produce reactive $•O_2^-$ and •OH species, which subsequently oxidize Fast Green molecules, while Cu modification can facilitate charge separation and suppress electron–hole recombination.

Fig. 2(c) depicts N_2 adsorption–desorption isotherms of the synthesized zinc–iron–copper oxide (ZFCO) nanoparticles. The material exhibited a type IV adsorption isotherm accompanied by an H4 hysteresis loop, showing the presence of slit-shaped pores generated by the aggregation of nanosized particles. The textural analysis showed a specific surface area (SBET) of 18.8 ± 0.1 $m^2\ g^{-1}$, an average pore diameter (Dp) of 13.9 ± 0.5 nm, and a pore volume (Vp) of 0.067 ± 0.001 $cm^3\ g^{-1}$, with a mesoporous nature of the nanostructure. Such porous characteristics favor the adsorption of Fast Green molecules and provide a greater number of active sites for photocatalytic reactions, thereby enhancing the generation of reactive oxygen species during dye degradation. The observed surface area is consistent with values commonly reported for mixed-metal oxide nanomaterials subjected to high-temperature calcination, where particle coalescence and crystal growth may partially reduce the accessible surface area while preserving the mesoporous framework.

The ZFCO nanoparticles exhibited a BET surface area of 18.8 ± 0.1 $m^2\ g^{-1}$, pore diameter of 13.9 ± 0.5 nm, and pore volume of 0.067 ± 0.001 $cm^3\ g^{-1}$. For comparison, previously reported $ZnFe_2O_4$ and Cu-modified $ZnFe_2O_4$ photocatalysts exhibited surface areas of 68.814 and 84.866 $m^2\ g^{-1}$, pore diameters of 15.821 and 15.228 nm, and pore volumes of 0.281 and 0.294 $cm^3\ g^{-1}$, respectively (Alshehri *et al.* 2024). Other $ZnFe_2O_4$ photocatalysts have shown a surface area of 23.5 $m^2\ g^{-1}$, pore diameter of 51.1 nm, and pore volume of 0.12 $cm^3\ g^{-1}$. Although the present ZFCO possesses a comparatively moderate surface area and pore volume, its mesoporous pore structure remains favorable for dye diffusion and accessibility of photocatalytically active sites.

The surface charge characteristics of the synthesized zinc–iron–copper oxide (ZFCO) nanoparticles revealed a zeta potential of −0.36 ± 0.03 mV, indicating a negatively charged surface that can promote favorable electrostatic interactions with Fast Green dye molecules and enhance their transport toward the catalyst surface. The pHZPC behavior illustrated in Fig. 2(d) was evaluated using the eleven-point method. The ZFCO nanomaterial exhibited a pHZPC value of approximately 6.70, suggesting that the surface remains positively charged under acidic conditions (pH < 6.42) and becomes negatively charged at alkaline pH values (pH > 6.42). Considering the charge characteristics of the dye and catalyst, a solution pH close to neutrality can facilitate adsorption and photocatalytic degradation by increasing the interaction among pollutant molecules and active sites of the nanocatalyst.

Optical band-gap energy was determined from the Tauc plot derived from diffuse reflectance measurements, as illustrated in Fig. 2(e). The synthesized zinc–iron–copper oxide (ZFCO) nanoparticles exhibited a band-gap of 2.44 eV, demonstrating effective absorption within the visible-light region. This reduced band-gap value enhances the utilization of solar irradiation and promotes efficient photoinduced charge transfer between the valence and conduction bands, thereby improving photocatalytic activity under visible-light exposure.

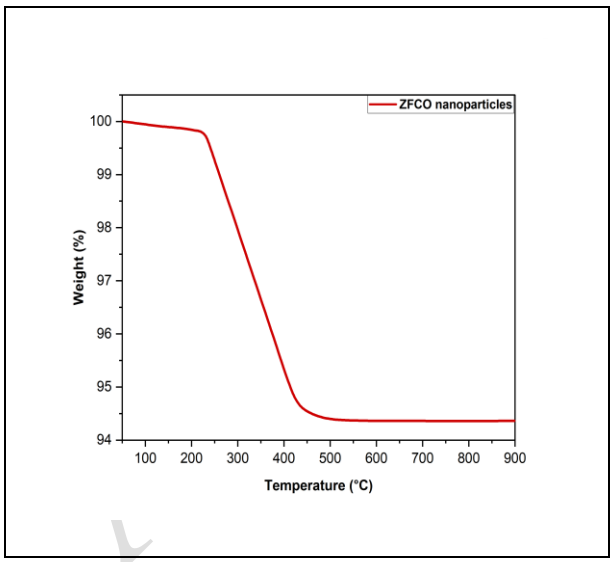

Fig. 3: Thermogravimetric analysis (TGA) profile of ZFCO nanoparticles

As illustrated in Fig. 3, the synthesized zinc–iron–copper oxide (ZFCO) nanoparticles exhibited two distinct weight-loss stages over the investigated temperature range. The initial mass reduction, observed between 50 and 220 °C, was attributed to the decomposition of residual organic compounds originating from the plant-mediated synthesis process, accounting for approximately 0.60% of the total weight loss. The subsequent loss observed mainly between 220 and 440 °C accounted for approximately 5.30% and was linked to the decomposition of residual organic compounds and strongly bound surface species within the mixed-metal oxide framework. The relatively low overall mass loss (5.90%) and high residual mass of approximately 94.10% indicate excellent thermal stability of the ZFCO nanostructures. Such behavior suggests that the material can maintain its structural integrity under elevated-temperature conditions, making it suitable for photocatalytic and related environmental applications.

The first mass-loss stage (50–220 °C, ~0.60%) was attributed to the removal of adsorbed moisture and weakly bound phytochemical residues, while the second stage (220–440 °C, ~5.30%) corresponded mainly to the decomposition of residual organic species derived from *Ocimum tenuiflorum*. In comparison with the previous study, $ZnFe_2O_4$ nanoparticles remained stable up to approximately 90 °C and exhibited ~2% mass loss between 400 and 850 °C due to residual organic decomposition and structural/crystallization changes (Rasheed-Adeleke *et al.* 2025). Although the present ZFCO exhibited a slightly higher total mass loss (~5.90%), its high residual mass (~94.10%) indicates good thermal stability of the mixed-metal oxide framework.

3.3. Experimental Design (CCRD 2^3) and Photocatalytic Degradation of Fast Green Dye

Table 3 summarizes the experimental results obtained from the CCRD 2^3 design for the photocatalytic degradation of FG dye by zinc–iron–copper oxide (ZFCO). The removal efficiency was strongly influenced by the combined effects of catalyst dosage, solution pH and dye concentration. Among the investigated experimental conditions, maximum degradation efficiency of 57.2% was achieved at FG concentration of 25 mg L^{-1}, a ZFCO nanoparticle dosage of 1.1 g L^{-1}, and solution pH of 4. Similarly, high degradation efficiencies of 53.8% and 51.5% were observed at pH values close to 2 and 4, respectively, highlighting the favorable influence of acidic conditions on the photocatalytic process. In contrast, lower removal efficiencies were recorded at alkaline pH and high dye concentrations, indicating reduced photocatalytic activity under such conditions. Based on experimental results, optimum operating conditions for Fast Green degradation were identified as an initial dye concentration of 25 mg L^{-1}, a catalyst dosage of 1.1 g L^{-1}, and a solution pH of 4, yielding a degradation efficiency of 57.2%. These optimized parameters were subsequently selected for further kinetic and mechanistic investigations of Fast Green removal using ZFCO nanoparticles.

Table 3. CCRD 2^3 design for fast green photodegradation using ZFCO nanoparticles

FG (mg L^{-1})	ZFCO-NPs (g L^{-1})	pH	%R
25	1.1	10	28.6
50	0.161	7	18.4
75	1.1	4	51.5
25	1.1	4	57.2
25	0.4	4	42.7
75	0.4	4	36.9
50	0.75	7	33
75	0.4	10	18.5
75	1.1	10	32.4
25	0.4	10	24.8
50	0.75	12.045	17.6
50	1.339	7	46.2
50	0.75	1.955	53.8
7.955	0.75	7	47.5
92.045	0.75	7	27.3
50	0.75	7	36.5
50	0.75	7	35.5

As illustrated in Fig. 4(a), the contour plot reveals the combined influence of Fast Green (FG) concentration and ZFCO nanoparticle dosage on removal efficiency at a fixed pH of 7. The degradation efficiency increased with increasing catalyst dosage, indicating a greater number of active surface sites for photocatalytic reactions. Conversely, increasing initial FG concentration resulted in a gradual decline in removal efficiency, which may be attributed to limited availability of reactive oxidative species and reduced light penetration at higher pollutant concentrations. The contour profile suggests that, the highest removal efficiencies were achieved at relatively low dye concentrations and elevated catalyst dosages, confirming the significant role of catalyst loading in enhancing photocatalytic performance.

Fig. 4(b) presents the predicted versus actual removal efficiencies obtained from developed quadratic RSM. The close distribution of the experimental data points around diagonal line demonstrates good agreement between observed and predicted values, indicating satisfactory model accuracy and reliability. Strong correlation among predicted and experimental responses confirms that the developed model adequately describes the photocatalytic degradation process within the investigated experimental domain and can be effectively used for process optimization and prediction of Fast Green removal efficiency.

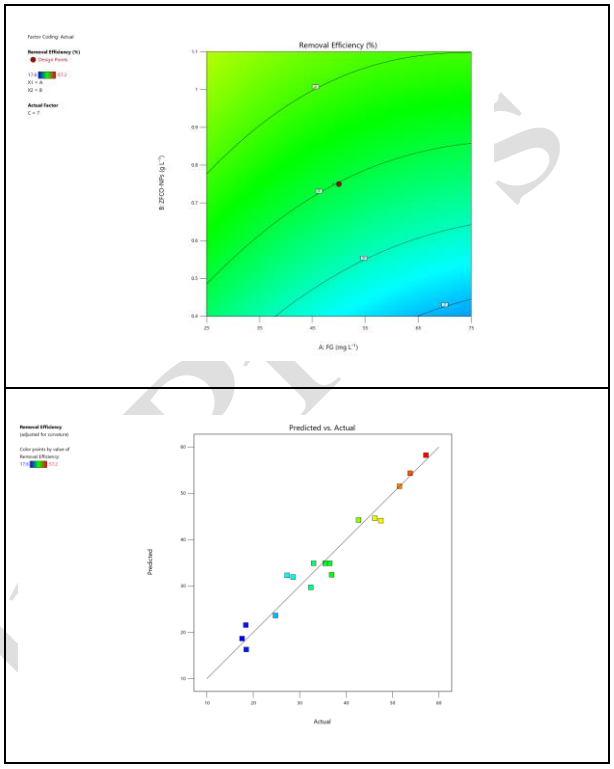

Fig. 4: (a) Contour plot showing the interaction between FG concentration and ZFCO nanoparticle dosage on FG removal efficiency at pH 7 and (b) Experimental versus predicted plot for the validation of quadratic RSM model

As summarized in Table 4, analysis of variance confirmed the adequacy and statistical significance of the quadratic model for Fast Green degradation using ZFCO nanoparticles. The model exhibited a high p-value of 0.0005 and an F-value of 17.89, showing that the regression model was statistically significant at the 95% confidence level. Among the investigated variables, solution pH ($F = 102.43$, $p < 0.0001$) exerted most significant influence degradation efficiency, followed by ZFCO nanoparticle dosage ($F = 42.71$, $p = 0.0003$) and FG concentration ($F = 11.23$, $p = 0.0122$). In contrast, the interaction terms (AB, AC, and BC) and quadratic terms (A^2, B^2, and C^2) were found to be statistically insignificant ($p > 0.05$). Furthermore, lack-of-fit test were not significant ($F = 6.06$, $p = 0.1476$), confirming developed model adequately represented experimental data within investigated design space. These results demonstrate that the individual effects of FG concentration, catalyst dosage, and pH predominantly governed photocatalytic degradation performance of Fast Green dye.

Table 4. ANOVA parameters (SS, df, MS, F_{cal}, F_{tab}, and R^2) for photocatalytic degradation of fast green dye

Source	Sum of Squares	df	Mean Square	F-value	p-value	
Model	2415.64	9	268.40	17.89	0.0005	significant
A-FG (mg L^{-1})	168.51	1	168.51	11.23	0.0122	
B-ZFCO-NPs (g L^{-1})	640.94	1	640.94	42.71	0.0003	
C-pH	1536.99	1	1536.99	102.43	< 0.0001	
AB	13.01	1	13.01	0.8667	0.3829	
AC	10.13	1	10.13	0.6748	0.4385	
BC	16.25	1	16.25	1.08	0.3327	
A^2	15.34	1	15.34	1.02	0.3457	
B^2	4.57	1	4.57	0.3047	0.5981	
C^2	3.60	1	3.60	0.2402	0.6390	
Residual	105.04	7	15.01			
Lack of Fit	98.54	5	19.71	6.06	0.1476	not significant
Pure Error	6.50	2	3.25			
Cor Total	2520.68	16				

3.3.1. Statistical Adequacy, Diagnostic Evaluation, and Experimental Validation of the Response-Surface Model

The statistical robustness of the quadratic response-surface model developed for Fast Green (FG) degradation using ZFCO nanoparticles was evaluated through analysis of variance (ANOVA), goodness-of-fit indicators, residual diagnostics, and independent experimental validation. The ANOVA results confirmed that the developed model was highly significant, with an F-value of 17.89 and a corresponding p-value of 0.0005, indicating that the probability of model significance due to random noise was less than 0.05%. This confirms that the regression model reliably captures the relationship between the independent variables and FG degradation efficiency at a 95% confidence level.

Among the investigated process variables, solution pH exhibited the most dominant influence on dye degradation, with an F-value of 102.43 ($p < 0.0001$), highlighting its critical role in governing surface charge interactions and catalytic activity of ZFCO nanoparticles. The second most influential factor was nanoparticle dosage ($F = 42.71$, $p = 0.0003$), followed by initial FG concentration ($F = 11.23$, $p = 0.0122$). In contrast, interaction effects (AB, AC, BC) and quadratic terms (A^2, B^2, C^2) were statistically insignificant ($p > 0.05$), suggesting that within the studied range, the system behavior is primarily governed by linear effects rather than strong synergistic or nonlinear interactions. The lack-of-fit test was also insignificant ($F = 6.06$, $p = 0.1476$), confirming that the model adequately represents the experimental data without systematic deviation.

The model's predictive capability was further supported by high goodness-of-fit statistics. The coefficient of determination ($R^2 = 0.9583$) indicates that 95.83% of the variability in FG removal efficiency is explained by the model. The adjusted R^2 (0.9048) confirms that the model remains reliable even after accounting for the number of predictors. Although the predicted R^2 (0.6894) is lower than the adjusted R^2, it still indicates acceptable predictive ability within the experimental domain, with a PRESS value of 782.96. The coefficient of variation (CV = 10.82%) reflects good experimental precision, while the Adequate Precision value of 14.12—well above the threshold of 4—confirms a strong signal-to-noise ratio, indicating that the model is suitable for navigating the design space.

Residual diagnostic analysis further validated model adequacy. The normal probability plot of internally studentized residuals showed an approximately linear distribution, confirming normality of errors, which was statistically supported by the Shapiro–Wilk test ($W = 0.9874$, $p = 0.9958$). Additionally, residuals plotted against predicted values exhibited random scatter around zero without discernible patterns, confirming homoscedasticity and independence of errors. All residuals remained within ±3, indicating the absence of influential outliers and reinforcing the reliability of the model.

Under optimized conditions (25 mg L^{-1} FG, 1.1 g L^{-1} ZFCO, pH 4), the model predicted a removal efficiency of 58.25%, with a 95% confidence interval of 50.75–65.75%.

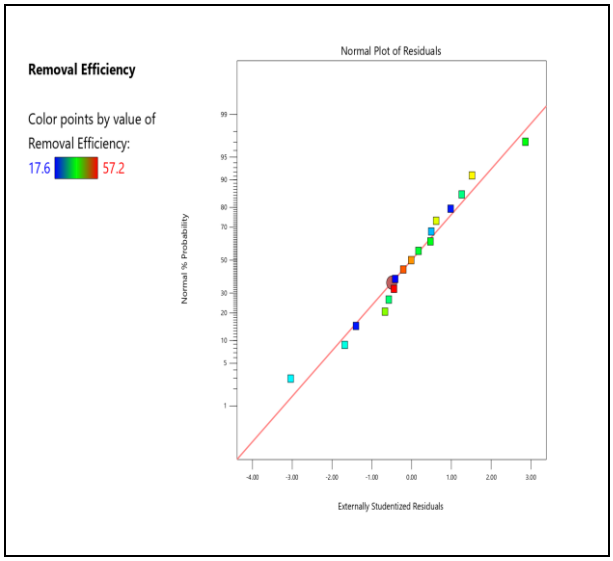

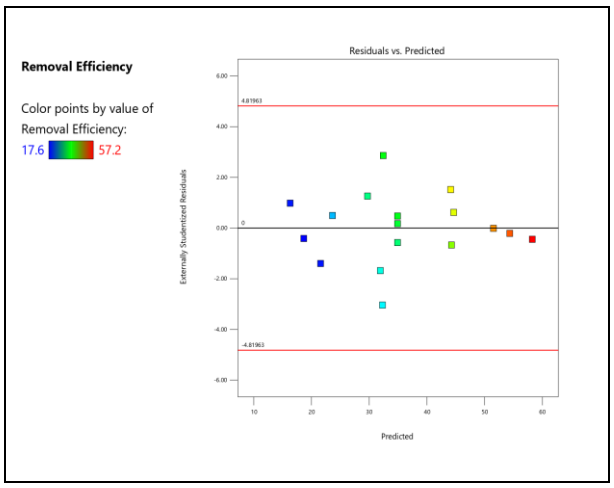

Fig. 5: Diagnostic plots of the quadratic model: (a) normal probability plot of internally studentized residuals and (b) internally studentized residuals versus predicted fast green removal efficiency

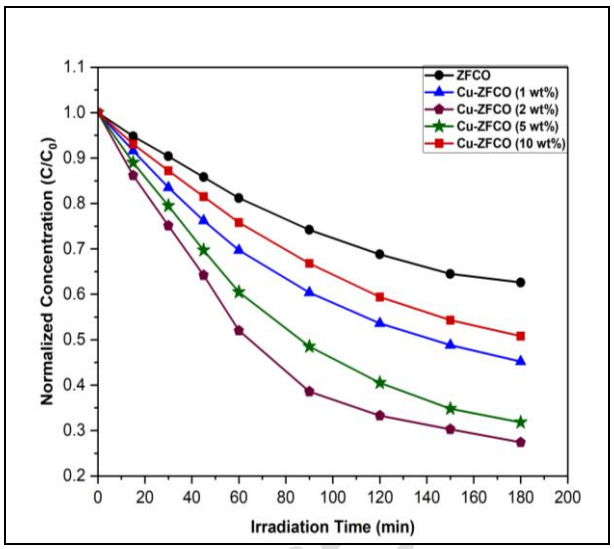

Fig.6: Photocatalytic degradation profiles of fast green (FG) dye under visible-light irradiation using pristine ZFCO and Cu-modified ZFCO nanocatalysts with different Cu loadings (1–10 wt.%)

3.4. Photocatalytic Analysis

As illustrated in Fig. 6, photocatalytic degradation of Fast Green dye by zinc–iron–copper oxide (ZFCO) followed pseudo-first-order reaction kinetics, exhibiting a constant rate of 0.003 min^{-1} with a correlation coefficient of 0.954 and achieving 37.5% dye removal after 180 min of visible-light irradiation. The relatively high molecular weight of Fast Green (808.9 g mol^{-1}) can hinder mass transfer and diffusion within the reaction medium, thereby limiting adsorption and photocatalytic degradation efficiency. Modification of the ZFCO nanocatalyst with 2 wt% copper species significantly enhanced photocatalytic performance, increasing the degradation efficiency to 73.0% and raising the kinetic constant from 0.003 to 0.0086 min^{-1}. The pristine ZFCO exhibited pseudo-first-order kinetics with k = 0.003 min^{-1} and R^2 = 0.954, whereas 2 wt.% Cu modification increased k to 0.0086 min^{-1}, corresponding to an approximately 2.9-fold enhancement in the apparent degradation rate. The relatively good linear fit supports the applicability of the pseudo-first-order kinetic model. The initial adsorption of Fast Green onto accessible ZFCO surface sites facilitates pollutant–catalyst interaction; however, under visible-light irradiation, the overall degradation is predominantly governed by surface photocatalytic reactions involving photogenerated charge carriers and reactive oxygen species. Thus, adsorption assists pollutant transfer to active sites, while the subsequent surface reaction primarily controls photocatalytic degradation. However, further increases in copper loading (5 and 10 wt%) resulted in a decline in degradation efficiency, which may be attributed to excessive surface coverage, particle agglomeration, and a reduction in the availability of active catalytic sites for photocatalytic reaction. A similar result/pattern is found in the literature (Ganesh *et al.* 2026).

The Cu-modified ZFCO exhibited 73.0% Fast Green degradation, which is moderate compared with recently reported $ZnFe_2O_4$-based photocatalysts showing approximately 91–99% degradation. For example, $CuO/ZnFe_2O_4$ achieved 91.13% Congo red degradation (Ravichandran *et al.* 2024), while $ZnFe_2O_4$@Co/Ni-MOF (Javed *et al.* 2024)and $ZnFe_2O_4$@g-C_3N_4 (Li *et al.* 2025)achieved 98.4% Congo red and 99.99% methylene blue degradation, respectively. The present study demonstrates promising photocatalytic performance for Fast Green degradation under the investigated conditions. While degradation efficiencies reported in the literature vary with pollutant characteristics, initial concentration, catalyst dosage, light intensity, pH, and irradiation time, the obtained results highlight the effectiveness of Cu-modified ZFCO for visible-light-driven dye degradation and support its potential for sustainable wastewater treatment applications. Although the present ZFCO shows moderate degradation efficiency, its plant-mediated synthesis, Cu-enhanced visible-light activity, and integration with RSM and ML provide advantages for sustainable photocatalytic process development.

The effect of nanocatalyst concentration on FG removal using pristine and Cu-modified ZFCO nanoparticles is presented in Fig. 7. Increasing catalyst concentration initially enhanced removal owing to the greater availability of surface-active sites. Maximum removal was observed at approximately 1.5–2.0 g L^{-1}, after which the efficiency decreased gradually, possibly because of particle agglomeration, increased light scattering and reduced photon penetration. Cu-modified ZFCO consistently exhibited higher removal efficiency than pristine ZFCO throughout the investigated concentration range.

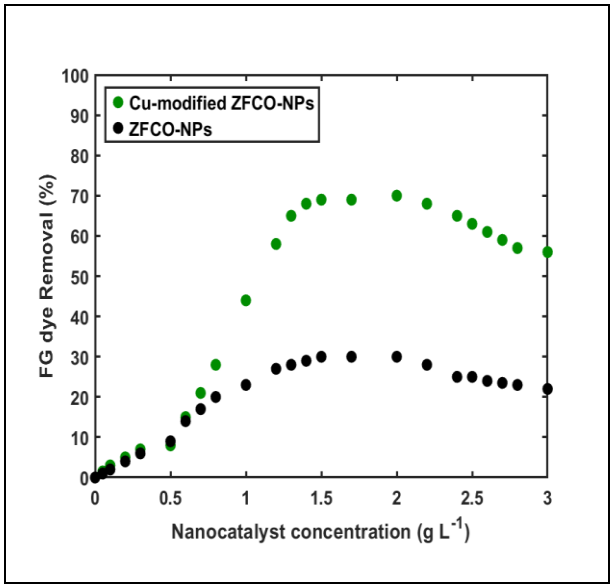

Fig. 7: Effect of nanocatalyst concentration on Fast Green removal using pristine and Cu-modified ZFCO nanoparticles

The enhanced photocatalytic activity following Cu modification is attributed to improved visible-light utilization, charge separation, and increased availability of active sites. However, this mechanism is proposed based on the observed photocatalytic and optical behavior. Further XPS, PL, EIS, and photocurrent measurements are required to directly verify Cu chemical states, charge-carrier recombination, interfacial resistance, and photoinduced charge-transfer behavior, respectively, and will be considered in future investigations.

3.5. Machine Learning

The predictive performances of GPR, SVR, random forest and LSBoost were reassessed using nested condition-wise cross-validation. Complete irradiation-time profiles belonging to the same FG–ZFCO–pH condition were retained within the same fold, preventing observations from an identical operating condition from occurring in both model training and testing. The resulting performance metrics are presented in Table 5.

Table 5. Nested condition-wise cross-validation performance of the machine-learning models for fast green removal

Model	Nested-CV R^2	Nested-CV RMSE	Nested-CV MAE	Nonzero-time R^2	Nonzero-time RMSE	Mean-condition RMSE
SVR	0.9156	4.2915	2.9627	0.8662	4.6234	3.6002
GPR–LSBoost ensemble	0.9031	4.5982	3.6055	0.8465	4.9536	–
GPR	0.8825	5.0625	3.8226	0.8154	5.4310	4.6366
LSBoost	0.8451	5.8122	4.4904	0.7536	6.2753	5.4268
Random forest	0.8224	6.2250	4.6421	0.7171	6.7238	5.8034

Among the evaluated models, SVR demonstrated the best generalization performance, achieving a nested cross-validation R^2 of 0.9156, RMSE of 4.2915 and MAE of 2.9627. After excluding the common initial measurements recorded at 0 min, SVR maintained an R^2 of 0.8662, RMSE of 4.6234 and MAE of 3.3535. Its mean condition-level RMSE was 3.6002, indicating satisfactory prediction of FG removal for operating conditions excluded from model training and hyperparameter optimization.

The leakage-free GPR–LSBoost ensemble produced the second-highest predictive performance, with an R^2 of 0.9031, RMSE of 4.5982 and MAE of 3.6055. The individual GPR model achieved an R^2 of 0.8825 and RMSE of 5.0625, whereas LSBoost and random forest produced R^2 values of 0.8451 and 0.8224, respectively. Consequently, SVR was selected as the best-performing model based on its lowest nested cross-validation RMSE. The lower performance values compared with those obtained from the original random training–testing split provide a more conservative and reliable estimate of model generalization.

As illustrated in Fig. 8, the SVR predictions were distributed comparatively close to the equality line throughout the investigated response range. GPR also demonstrated satisfactory agreement between the experimental and predicted responses, whereas LSBoost and random forest showed greater deviations, particularly at higher removal efficiencies. These results confirm the importance of evaluating model performance using complete held-out operating-condition groups.

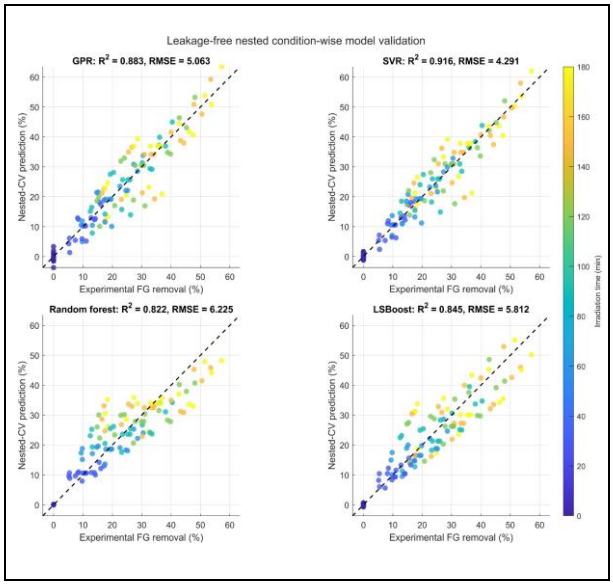

Fig. 8: Experimental versus nested cross-validated predictions of Fast Green removal using GPR, SVR, random forest and LSBoost models

Permutation feature importance was applied to interpret the selected SVR model, as shown in Fig. 9. Irradiation time produced the greatest increase in RMSE after permutation and was therefore identified as the dominant predictive variable. This was followed by solution pH, ZFCO dosage and initial FG concentration. These values represent model-based predictive importance and should not be interpreted independently as direct causal effects.

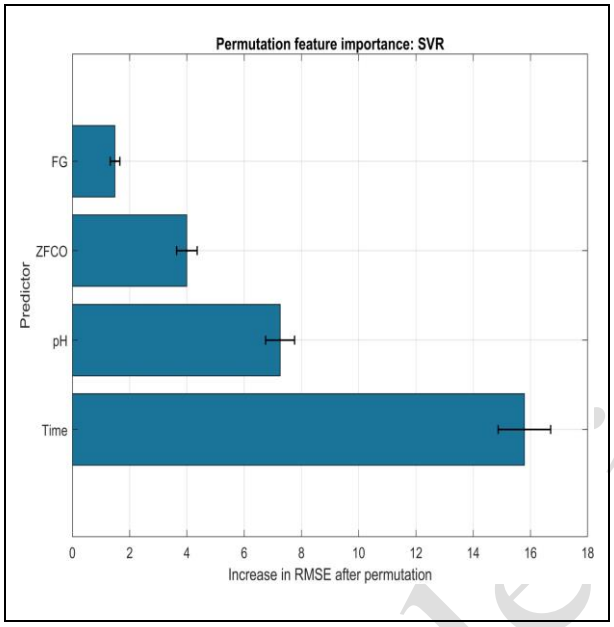

Fig. 9: Permutation importance of FG concentration, ZFCO dosage, pH and irradiation time for the selected SVR model

The partial-dependence sensitivity profiles further illustrate the model response to the investigated variables. Predicted FG removal increased with irradiation time and ZFCO dosage, whereas increasing initial FG concentration and solution pH generally reduced the predicted response. These patterns were consistent with the experimental and response-surface findings, which identified acidic conditions, lower dye concentration and adequate catalyst loading as favourable for FG degradation.

The learning behaviour and architecture of the MLP–ANN are presented in Fig. 10. The network consisted of four input neurons, one hidden layer containing 10 neurons and one output neuron representing FG removal efficiency. A rapid decrease in MSE was observed during the initial training epochs, followed by gradual convergence, indicating effective learning. Early stopping based on validation performance was used to reduce overfitting. Because the ANN was evaluated using a 70:15:15 training–validation–testing partition rather than the nested condition-wise procedure, its performance was interpreted separately and was not directly ranked against the nested cross-validation results in Table 5.

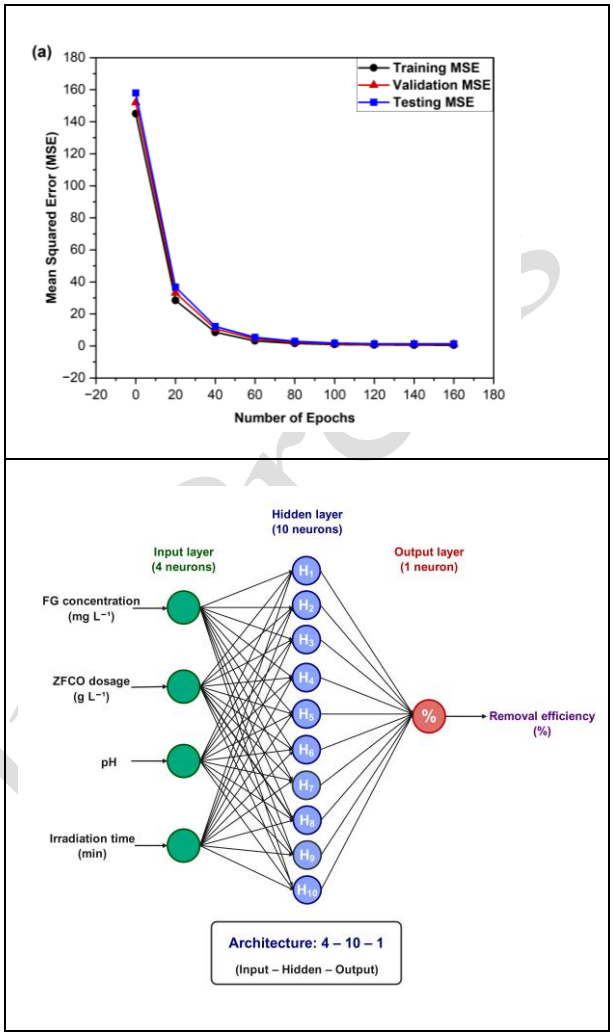

Fig. 10: Optimized MLP–ANN model: (a) training, validation and testing MSE profiles and (b) selected 4–10–1 neural-network architecture

Therefore, model generalization was assessed using nested condition-wise cross-validation, in which complete operating-condition groups were excluded from model training and hyperparameter optimization.

3.6. Phytotoxicity Evaluation of ZFCO Nanoparticles and Cu-modified ZFCO Nanoparticles

Fig. 11(a–b) presents the phytotoxicity assessment of ZFCO nanoparticles toward *Vigna radiata* and *Triticum aestivum* after 78 h of exposure. A concentration-dependent decrease in root elongation was observed for both plant species with increasing nanoparticle concentration. For *Vigna radiata*, root length decreased from approximately 8.2 cm in the control to 5.0 cm at 200 mg L^{-1}, corresponding to a

reduction of about 39.0%. Similarly, *Triticum aestivum* exhibited a decrease in root elongation from approximately 10.5 cm to 6.7 cm, representing a reduction of about 36.2%. The observed inhibition may be attributed to nanoparticle–root interactions that affect nutrient uptake, water transport, and cellular growth processes. Similarly, Nickel-zinc ferrite (Ni-ZF, $Ni_xZn_{1-x}Fe_2O_4$) nanoparticles were synthesized via co-precipitation for the photocatalytic degradation of the pharmaceutical pollutant diclofenac. The nanoparticles achieved nearly 99% degradation within 50 minutes at neutral pH, while toxicity studies confirmed the treated water was safe for microbial and plant growth (Mohan *et al.* 2022). These findings suggest that increasing concentrations of ZFCO nanoparticles exert measurable phytotoxic effects on early root development in both plant species.

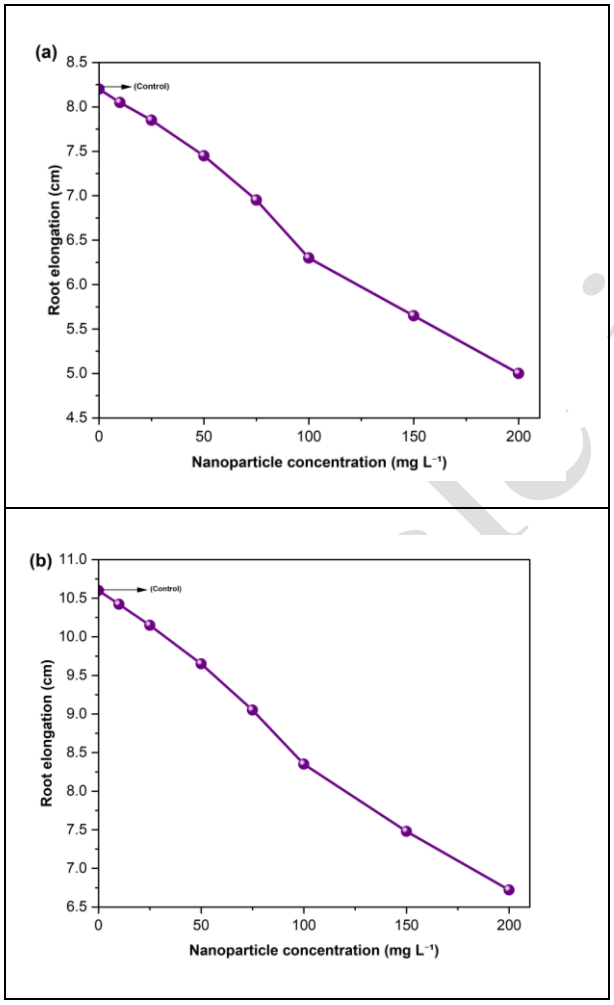

Fig. 11: Effect of ZFCO nanoparticle concentration on root elongation of (a) *Vigna radiata* and (b) *Triticum aestivum* after 78 h of exposure

In addition to root elongation, germination percentage, chlorophyll content, and plant biomass are important indicators for comprehensive phytotoxicity assessment. These parameters provide complementary information regarding seed viability, photosynthetic response, and overall plant growth following nanoparticle exposure. Statistical evaluation using ANOVA ($p < 0.05$) is also recommended to determine the significance of concentration-dependent effects. Although the present study demonstrates concentration-dependent changes in root elongation, these additional endpoints will be investigated in future studies to provide a more comprehensive assessment of the environmental safety of ZFCO and Cu-modified ZFCO nanoparticles.

4. CONCLUSIONS

This research investigated photocatalytic degradation of Fast Green dye by zinc–iron–copper oxide (ZFCO) and copper-modified ZFCO nanocatalysts under visible-light irradiation. Comprehensive characterization through XRD, FTIR, N_2 adsorption–desorption analysis, zeta potential measurements, and SEM confirmed the successful synthesis of nanostructured photocatalysts with favorable physicochemical properties for dye degradation applications. Copper modification significantly enhanced the photocatalytic activity of ZFCO nanoparticles, increasing the predicted Fast Green removal efficiency from approximately 30% for the unmodified catalyst to nearly 70% at an optimum catalyst concentration of 1.5–2.0 g L^{-1}.

The effects of dye concentration, catalyst dosage, and solution pH were systematically evaluated using a Central Composite Rotatable Design (CCRD 2^3) coupled with response surface methodology. ANOVA confirmed the statistical significance of the developed quadratic model, with solution pH identified as an influential operating parameter, followed by catalyst dosage and dye concentration. The optimum experimental conditions corresponded to a Fast Green concentration of 25 mg L^{-1}, ZFCO nanoparticle dosage of 1.1 g L^{-1}, and a solution pH of 4, resulting maximum degradation efficiency of 57.2%.

Among the evaluated machine-learning algorithms, SVR provided the best generalization performance under nested condition-wise cross-validation, achieving an R^2 of 0.9156, RMSE of 4.2915 and MAE of 2.9627. Permutation importance identified irradiation time as the dominant predictive variable, followed by solution pH, ZFCO dosage and FG concentration. The observed sensitivity trends were consistent with the experimental and response-surface findings.

Overall, Cu modification improved the photocatalytic performance of ZFCO, demonstrating its potential for visible-light-assisted Fast Green removal, although the achieved degradation efficiency remains moderate. The integration of green synthesis, RSM optimization, and ML prediction provides a useful framework for photocatalytic process development.

Future studies should evaluate the catalyst using real industrial wastewater, quantify TOC removal and mineralization efficiency, investigate catalyst recovery and recyclability over repeated cycles, identify degradation intermediates, and conduct pilot-scale validation to establish its practical applicability for wastewater treatment.

FUNDING

This research received no specific grant from any funding agency in the public, commercial, or not-for-profit sectors.

CONFLICTS OF INTEREST

The authors declare that there is no conflict of interest.

COPYRIGHT

REFERENCES

Ali, H., Yasir, M., Haq, H. U., Guler, A. C., Masar, M., Khan, M. N. A., Machovsky, M., Sedlarik, V. and Kuritka, I., Machine learning approach for photocatalysis: An experimentally validated case study of photocatalytic dye degradation, *J. Environ. Manage.*, 386, 125683(2025). https://doi.org/10.1016/j.jenvman.2025.125683

Alshehri, A., Alharbi, L., Wani, A. A. and Malik, M. A., Biogenic Punica granatum flower extract assisted $ZnFe_2O_4$ and $ZnFe_2O_4$-Cu composites for excellent photocatalytic degradation of RhB dye, *Toxics*, 12(1), 77(2024). https://doi.org/10.3390/toxics12010077

Amar, I. A., Nouh, A. A., Aljarani, A. M., Shamsi, S. S., Ghosh, K. S. and Hosseini-Bandegharaei, A., Surfactant-assisted co-precipitation synthesis of Zn-doped tin ferrite for methylene blue and Congo red dyes photodegradation and phytotoxicity studies, *Chem. Africa*, 8(10), 5555–5588(2025). https://doi.org/10.1007/s42250-025-01472-0

Azam, Q. M., Yaqoob, A., Ali, S. K., Alamri, A. A., Hassan, K. F., Imran, M. and Nawaz, S., Exploring the multifunctionality of co-doped (Zn,Co)-CuO nanoparticles through biological activities, photodegradation, and biotoxicity assessment, *J. Sol-Gel Sci. Technol.*, 115(3), 1852–1866(2025). https://doi.org/10.1007/s10971-025-06894-3

Bernegossi, A. C., Freitas, B. L. S., Castro, G. B., Marques, J. P., Trindade, L. F., de Lima e Silva, M. R., Felipe, M. C. and Ogura, A. P., A systematic review of the water treatment sludge toxicity to terrestrial and aquatic biota: State of the art and management challenges, *J. Environ. Sci. Health A*, 57(4), 282–297(2022). https://doi.org/10.1080/10934529.2022.2060021

de Morais, E. B., Nascimento, M. X., de Vasconcelos, L. G., Golin, R., Lopes, P. R. M., Ambrosio, J. A. R. and Simioni, A. R., Exploring the Dipteryx alata fruit endocarp as a novel source for the synthesis of silver nanoparticles: Antibacterial and photocatalytic insights for water purification, *J. Water Sanitation Hygiene Develop.*, 14(7), 552–564(2024). https://doi.org/10.2166/washdev.2024.025

Ganesh, C. U. C., Krushna, B. R. R., Navya, N., Sharma, S. C., Vickneshwaran, V., Thangamani, K., Mohapatra, S. S., Ray, S., Manjunatha, K., Wu, S. Y., Yu, S. L., Galivarapu, J. K., Ramakrishna, G., Arunakumar, R., Nagabhushana, H. and Al-Asbahi, B. A., Sustainable synthesis of V_2O_5:Sm^{3+} nanoparticles for malachite green photodegradation and high-efficiency supercapacitors, *J. Taiwan Inst. Chem. Eng.*, 178, 106341(2026). https://doi.org/10.1016/j.jtice.2025.106341

Javed, K., Abbas, N., Bilal, M., Alshihri, A. A., Rab Nawaz, H. Z., Ramadan, M. F. and Naqvi, S. A. R., Fabrication of a $ZnFe_2O_4$@Co/Ni-MOF nanocomposite and photocatalytic degradation study of azo dyes, *RSC Adv.*, 14(42), 30957–30970(2024). https://doi.org/10.1039/d4ra05283h

Kaur, J., Kaur, P., Garg, T., Kumar, V., Tikoo, K., Singh, B., Paulik, C., Kaushik, A. and Singhal, S., Synchronized sensing and annihilation of virulent organo-contaminants in water bodies using a highly fluorescent novel nanohybrid of Tulsi (*Ocimum tenuiflorum*) leaves derived carbon dots and $NiFe_2O_4$ nanoparticles, *Sustain. Mater. Technol.*, 35, e00561(2023). https://doi.org/10.1016/j.susmat.2022.e00561

Kumar, A., Poornima, S. N., Subbulakshmi, R., Selvaraju, M., G, R. K. and Jayabalan, C., Hierarchical green carbon fibers from banana pseudostem for efficient Pb^{2+} adsorption: Kinetics, isotherms, and machine learning prediction, *Interact.*, 247(1), 188(2026). https://doi.org/10.1007/s10751-026-02534-6

Lakshmi, H., Rasal, R. K., Badsha, I. and Devasena, T., A smart cubebinol–CuO nanocomposite for dual electrochemical sensing and visible-light-driven photodegradation of tetracycline: Box–Behnken optimization, mechanistic insight and kinetics, *Environ. Sci. Pollut. Res.*, 32(24), 14614–14631(2025). https://doi.org/10.1007/s11356-025-36514-0

Li, L., Jianhua, W. and Fang, H., Fabrication of $ZnFe_2O_4$@g-C_3N_4 for enhanced photo-Fenton effect and visible light-driven organic dye degradation, *Sci. Rep.,* 15(1), 21707(2025). https://doi.org/10.1038/s41598-025-05096-9

Lian, J., Wu, J., Zeb, A., Zheng, S., Ma, T., Peng, F., Tang, J. and Liu, W., Do polystyrene nanoplastics affect the toxicity of cadmium to wheat (Triticum aestivum L.)?, *Environ. Pollut.,* 263, 114498(2020). https://doi.org/10.1016/j.envpol.2020.114498

Liaqat, A., Bibi, I., Kamal, S., Raza, Q., Mustafa, G., Lim, S., Ajmal, K., Alwadai, N., Nazir, A. and Iqbal, M., Band gap engineering in Cu-substituted $ZnCo_2O_4$ spinel nanoparticles: Experimental and DFT insights into photocatalytic and antimicrobial performance, *J. Alloys Compd.,* 1071, 188766(2026). https://doi.org/10.1016/j.jallcom.2026.188766

Ma, Z. Q., Xu, Y. C., Fan, Z. J., Hou, D. Y. and Xu, Q. Y., Impacts of cuprous oxide nanoparticles on wheat root morphology and genotoxicity, *J. Appl. Eco*., 32(3), 1105–1111(2021). https://doi.org/10.13287/j.1001-9332.202103.031

Mahmud, H. A., Oviedo, L. R., da Silva, M. D. C. R., dos Santos, C., Pavoski, G., Tenório, J. A. S., Espinosa, D. C. R. and da Silva, W. L., Visible-light photocatalytic activity of a green niobium pentoxide nanocatalyst: Experimental analysis and machine learning approach, *J. Photochem. Photobiol. A Chem.,* 469, 116585(2025). https://doi.org/10.1016/j.jphotochem.2025.116585

Makofane, A., Motaung, D. E. and Hintsho-Mbita, N. C., Photocatalytic degradation of methylene blue and sulfisoxazole from water using biosynthesized zinc ferrite nanoparticles, *Ceram. Int.,* 47(16), 22615–22626(2021). https://doi.org/10.1016/j.ceramint.2021.04.274

Mohan, H., Muthukumar Sathya, P., Vadivel, S., Ha, G. H., Oh, H. S., Kim, G., Seralathan, K. K. and Shin, T., Highly efficient visible light photocatalysis of $Ni_xZn_{1-x}Fe_2O_4$ (x = 0, 0.3, 0.7) nanoparticles: Diclofenac degradation mechanism and eco-toxicity, *Chemosphere,* 301, 134699(2022). https://doi.org/10.1016/j.chemosphere.2022.134699

Mondal, I., Halder, P., Biswas, S., Sau, S., Ghosh, S., Sultana, S., Chatterjee, R. K., Mondal, D., Paul, P. K. and Das, S., Flexible and reusable piezo-responsive ternary bionanocomposite membrane for energy generation and catalytic removal of organic pollutants, *J. Mater. Chem. A,* 14(13), 7747–7765(2026). https://doi.org/10.1039/d5ta09714b

Nithya, V. and Chirsabesan, B., Synthesis of copper-doped metal nanoferrites for efficient removal of pharmaceutical wastewater pollutants in membrane bioreactor system, *Asian J. Chem*., 36(10), 2391–2396(2024). https://doi.org/10.14233/ajchem.2024.32340

Rasheed-Adeleke, A. A., Olatunde, O. C., Seheri, N. H., Oyewo, O. A., Ferjani, H. and Onwudiwe, D. C., Synthesis and photocatalytic performance of $ZnFe_2O_4$ on the degradation of tetracycline in water, *Appl. Phys. A,* 131(8), 625(2025). https://doi.org/10.1007/s00339-025-08753-y

Ravichandran, D., Abdullah, M. M. S., Vasanthakumar, V., Ranjith, R., Suganya, S., Meena, R. and Murugesan, S., Ulva lactuca L. extract bio-templated fabrication of CuO/$ZnFe_2O_4$ nanocomposites for photodegradation organic dye pollutants and in vitro biological activities, *Colloids Surf. A Physicochem. Eng. Asp.,* 689, 133701(2024). https://doi.org/10.1016/j.colsurfa.2024.133701

Sabira, O., Drisya, N., Ajaykumar, A. P., Mathew, A., Narayanan Jayaraj, K., Binitha, V. S., Zeena, K. V., Roy, K. B., Janish, P. A., Sheena, P. and Viswanathan, K. P., From Ficus recemosa leaf galls to therapeutic silver nanoparticles: Antibacterial and anticancer applications, *Pharma.,* 16(8), 1025(2024). https://doi.org/10.3390/pharmaceutics16081025

Sathish, M., Sathana, V., Venkatesan, A., Amalraj, S. D., Gaspar, A., Julie, M. M. and Jayaprakash, J., Sustainable industrial wastewater treatment and antibacterial activity using environmental friendly ferrite nanoparticles, *Asian J. Chem*., 36(2), 377–383(2024). https://doi.org/10.14233/ajchem.2024.30882

Wouters, R. D., Druzian, D. M., Muraro, P. C. L., da Silva, M. D. C. R., dos Santos, C., Ruiz, Y. P. M., Galembeck, A., Pavoski, G., Espinosa, D. C. R. and da Silva, W. L., TiO_2-NPs/ZnO-NPs@Co_3O_4 nanocomposite from natural extracts for the Rhodamine 6G photodegradation, *Surf. Interf*., 48, 104282(2024). https://doi.org/10.1016/j.surfin.2024.104282